Supporting Information

Highly Dispersed Antenna-Single-Atom-Reactor on Metal-Organic Frameworks Support for Efficient Photocatalytic CO_2 Reduction

Xi Chen[†a,b], Yanhui Su[†a,b], Zhangyi Zheng[a,b], Jinzhou Chen[a,b], Tong Zhou[a,b], Zhihe Wei[*a,b], Wenjun Yang[*a,b], Zhao Deng[a,b], Yang Peng[*a,b]

[a] *Soochow Institute for Energy and Materials Innovations, College of Energy, Key Laboratory of Advanced Carbon Materials and Wearable Energy Technologies of Jiangsu Province, Soochow University, Suzhou 215006, P. R. China.*

[b] *Jiangsu Key Laboratory of Advanced Negative Carbon Technologies, Soochow University, Soochow 215123, P. R. China.*

[*] E-mail: wjyang@suda.edu.cn (W. Yang); ypeng@suda.edu.cn (Y. Peng)

1. Experimental details

Synthesis of UiO-66-$(SH)_2$: By dissolving $ZrCl_4$ (96 mg, 0.41 mmol) and compound H_2DMBD (95mg, 0.41 mmol) in a mixed solution (3.4 mL acetic Acid and 16 mL DMF), the yellow clarifying solution was poured into a 50 mL single-necked flask. The solution was vacuumed and filled with argon three times for 10 min each time to completely remove oxygen, and then placed in an oil bath at 120 ℃ for 24 h. After cooling to room temperature, the solution was washed three times with DMF, then three times with ethanol, and vacuum dried overnight at 60 ℃. Collect yellow powder for later use. The prepared UiO-66-$(SH)_2$ powder sample was dispersed into a solution containing methanol and stirred for 3 h. A similar procedure was then performed (also lasting 3 h) by using methylene chloride instead of methanol. The solids were vacuum-dried in a tubular furnace at 150 °C to obtain an activated UiO-66-$(SH)_2$ sample.

Synthesis of Ag@UiOS: Silver nitrate (128 mg) was dissolved in a mixture containing 0.5 mL of deionized water and 2.5 mL of ethanol, then the Ag salt solution was quickly poured into a glass vial containing 100 mg of activated UiO-66-$(SH)_2$ to produce a slurry. The Ar gas was drummed to remove oxygen from the solution, treated with ultrasound for 5 min to ensure adequate dispersion, and then stirred strongly at room temperature for 16 h. After thoroughly removing excess unbound Ag ions, vacuum drying at 150 ℃ for 16 h. The resulting sample was designated Ag@UiOS.

Synthesis of Cu@UiOS: After 12 h of 40 mg of UiO-66-$(SH)_2$ in a vacuum oven at 150 °C, it was added to 8 mL of water and homogeneously dispersed by sonication. Subsequently, 10 mg of copper nitrate ($Cu(NO_3)_2$) was added and stirred for 3.5 h at 10 °C in a vacuum state. Afterward, excess precursors were removed by ethanol centrifugation and dispersed into a mixed solution containing 2 mL of ethanol and 8 mL. Wash twice with ethanol centrifugation after 1 h of light at 300 W xenon lamp for 15 A, after the end of the reaction. Finally, vacuum drying is performed at 60 °C for later use, the prepared samples were named Cu@UiOS.

Synthesis of $AgCu_{0.47}$@UiOS: First, 100 mg of Ag@UiOS is dispersed by sonication into 8 mL of deionized water. In the meantime, dissolve 10 mg of copper nitrate in 2 mL of water. The copper nitrate solution was mixed with the Ag@UiOS suspension with continuous agitation (10 °C, 500 rpm) for a reaction time of 12 h. After the reaction, the sample is washed twice with ethanol to remove excess

solution and impurities. Finally, overnight vacuum drying at 60 °C yields the final AgCu@UiOS material. In addition, samples with different copper content gradients were prepared by adjusting the input of copper nitrate (5, 10, 20, and 40 mg) and named $AgCu_{0.21}$@UiOS, $AgCu_{0.47}$@UiOS, $AgCu_{0.58}$@UiOS, and $AgCu_{0.66}$@UiOS with the Cu content measured by ICP-AES, respectively.

Materials Characterization. The morphology and microstructure of the products were characterized by scanning electron microscopy (SEM, Hitachi SU8010) and spherical aberration-corrected transmission electron microscope (ACTEM, FEI Titan Themis Cubed G2 300) equipped with an energy-dispersive X-ray analyzer (EDS). Powder X-ray diffraction (XRD) patterns were recorded on a Bruker D8 Advance X-ray diffractometer with a Cu K source (λ=0.15406 nm). X-ray photoelectron spectroscopy (XPS, Thermo Fisher, Escalab 250Xi) was used to detect the surface composition and chemical state of the material, and all binding energy values were calibrated with C1s=284.6 eV. The Brunauer-Emmett-Teller specific surface area (S_{BET}) was conducted on the Micromeritics ASAP 2460. Raman spectroscopy was acquired using a confocal laser Raman microscope (Horiba Jobin Yvon, HR Evolution). Inductively coupled plasma atomic emission spectrometry (ICP-AES) and an OPTIMA 8000 analyzer (Perkin Elmer Inc.) were used to detect the metal ion content. The photoluminescence (PL) spectra were obtained by an FLS1000 photoluminescence spectrometer. UV-vis diffuse reflectance spectra (DRS) were recorded by a SHIMADZU UV-2600 spectrophotometer using $BaSO_4$ as the reference. The X-ray absorption near-edge structure (XANES) and extended X-ray absorption fine structure (FT-EXAFS) data were collected at the 11B line station of the Shanghai Synchrotron Radiation Source.

Photocatalytic CO_2 Reduction. The photocatalytic activity of the obtained catalysts was evaluated in a solid-gas reaction system in a 180 mL stainless steel container. Use a 300 W xenon arc lamp with an AM 1.5 filter as the light source. Disperse 5 mg catalyst powder into 1.5 mL ethanol solution, evenly coated on the glass support, bake at 100 ℃ for 0.5 h, put it into a container, add 2 mL deionized water, and press it with a seal. During the test, high purity CO_2 gas was flushed three times. Then, fill the container with CO_2 until the system pressure reaches 0.3 MPa. Finally, turn on the Xe light and start calculating the reaction time. Gas products from the reactor are added to GC at 4 h intervals for detection of reaction products.

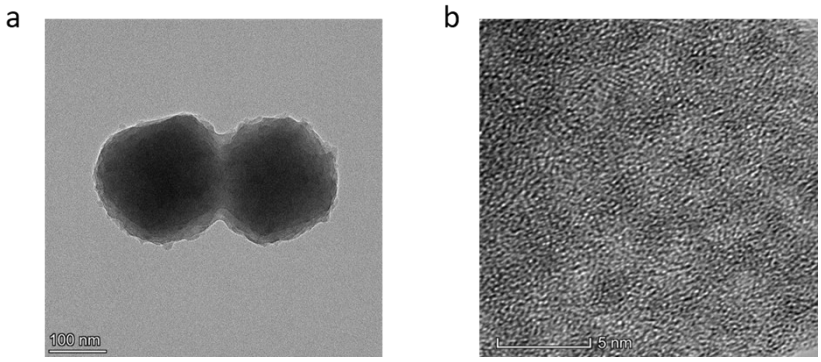

Figure S1. (a) TEM and (b) Cross-sectional AC-TEM image of UiO-66-$(SH)_2$.

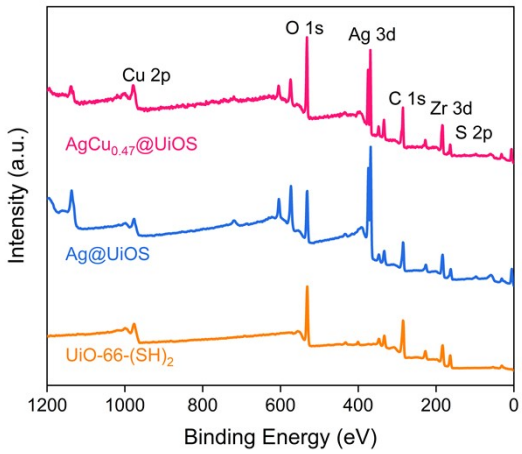

Figure S2. XPS survey of UiO-66-$(SH)_2$, Ag@UiOS and $AgCu_{0.47}$@UiOS.

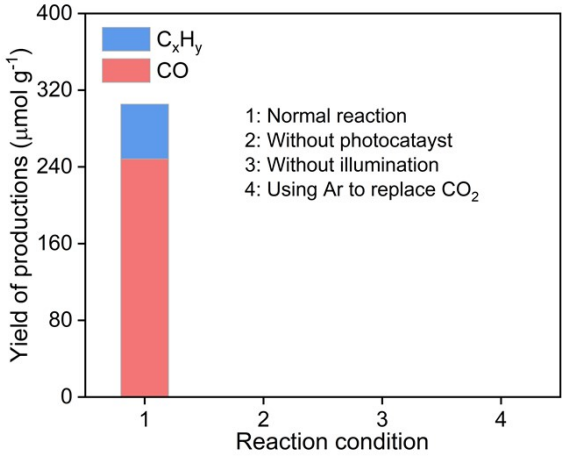

Figure S3. Photocatalytic experiments under various control conditions.

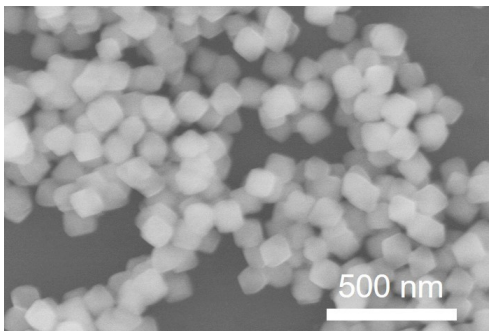

Figure S4. SEM image of post-cycling $AgCu_{0.47}$@UiOS.

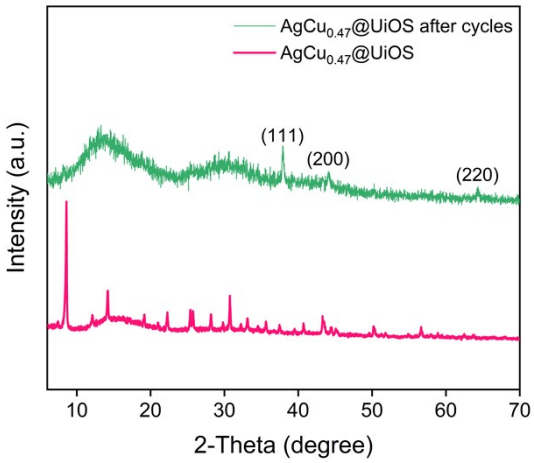

Figure S5. XRD spectra of $AgCu_{0.47}$@UiOS and post-cycling $AgCu_{0.47}$@UiOS.

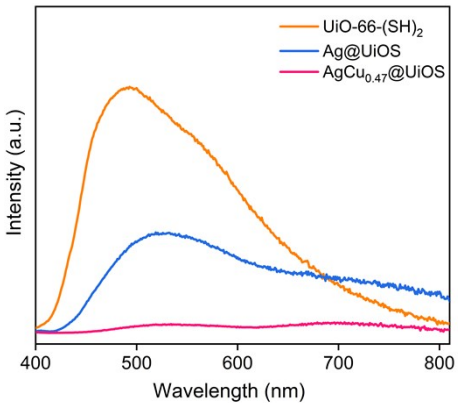

Figure S6. Steady-state photoluminescence spectra (ss-PL) of UiO-66-$(SH)_2$, Ag@UiOS and $AgCu_{0.47}$@UiOS.

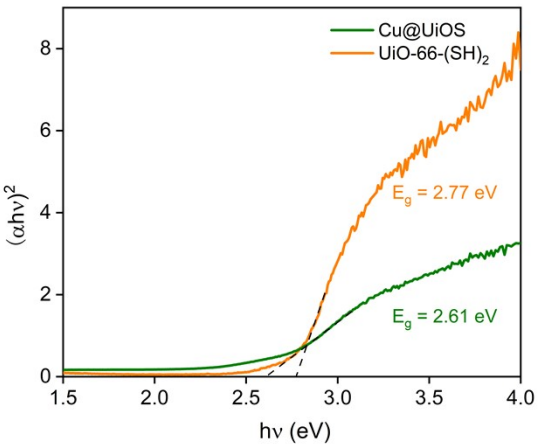

Figure S7. UV/Vis Tauc plots of the UiO-66-$(SH)_2$, and Cu@UiOS.

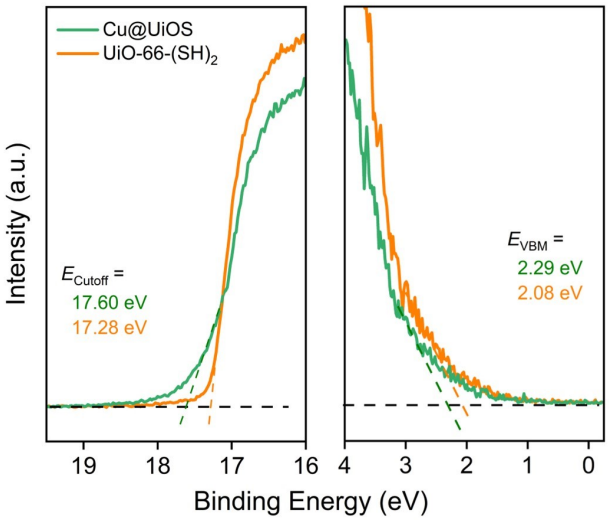

Figure S8. UPS spectra of the UiO-66-$(SH)_2$, and Cu@UiOS.

Table S1. Ag and Cu contents determined by ICP-MS for $AgCu_X$@UiOS.

Catalysts	Mass fraction of Ag (%)	Mass fraction of Cu (%)	The molar ratios of Cu/Ag (%)
$AgCu_{0.21}$@UiOS	39.8	0.21	0.21
$AgCu_{0.47}$@UiOS	39.8	0.47	0.47
$AgCu_{0.58}$@UiOS	39.8	0.58	0.58
$AgCu_{0.66}$@UiOS	39.8	0.66	0.66

Table S2. Comparison of the production rates toward artificial photosynthesis without using sacrificial agent.

Photocatalysts	Light	CO evolution rate (μmol g^{-1} h^{-1})	C_xH_y evolution rate (μmol g^{-1} h^{-1})	Total electron rate (μmol g^{-1} h^{-1})	Reference
UiO-66/Co_9S_8	IR	/	25.7	205.6	1
BTOPAu	300 W xenon lamp	34.15	/	68.3	2
c-CSON	IR	21.95	4.11	76.78	3
$Bi_{19}Br_3S_{27}$	Visible light	/	17.2	137.6	4
ZnO/g-C_3N_4	300 W xenon lamp	0.85	/	1.7	5
Vs-$CuIn_5S_8$	Visible light	/	8.7	69.6	6
UiO-66-6	300 W xenon lamp	1.33	/	2.66	7
$SrBi_2Nb_2O_9$	300 W xenon lamp	/	8.75	70	8
TTCOF-Zn	Visible light	2.06	/	4.12	9
Cu/carbon nitride	300 W xenon lamp	11.21	2.36	37.8	10
Pt-defective CN	300 W xenon lamp	/	6.3	50.4	11
Pt@h-BN	300 W xenon lamp	/	9.2	73.6	12
ZnSe/CdS dot-on-rods	400 nm LEDs	11.3	/	22.6	13
MTCN-H	300 W xenon lamp （300-1200 nm）	16.87	/	33.74	14
NNU-31-Zn	300 W xenon lamp	/	26.3	52.6	15
CdS: Dy^{3+}/g-C_3N_4	300 W xenon lamp	23.4	8.06	111.28	16
FeTCP-OH-Co	300 W xenon lamp	0.396	17.72	36.23	17
Cu_2O@$Cu_3(BTC)_2$	500 W xenon lamp	/	0.09	0.72	18

BiOCl with Bi vacancies	300 W xenon lamp	21.99	/	43.98	19
$AgCu_{0.47}$@UiOS	300 W xenon lamp	**62**	**14.3**	**238.4**	**This Work**

[1] Yang S, Byun W J, Zhao F, et al. CO_2 enrichment boosts highly selective infrared-light-driven CO_2 conversion to CH_4 by UiO-66/Co_9S_8 photocatalyst. *Advanced Materials*, **2024**: 2312616.

[2] Liu L, Hu J, Ma Z, et al. One-dimensional single atom arrays on ferroelectric nanosheets for enhanced CO_2 photoreduction. *Nature Communications*, **2024**, *15*(1): 305.

[3] Li X, Li L, Chen G, et al. Accessing parity-forbidden d-d transitions for photocatalytic CO_2 reduction driven by infrared light. *Nature Communications*, **2023**, *14*(1): 4034.

[4] Li J, Pan W, Liu Q, et al. Interfacial engineering of $Bi_{19}Br_3S_{27}$ nanowires promotes metallic photocatalytic CO_2 reduction activity under near-infrared light irradiation. *Journal of the American Chemical Society*, **2021**, *143*(17): 6551-6559.

[5] Chen C, Jin J, Chen S, et al. In-situ growth of ultrafine ZnO on g-C_3N_4 layer for highly active and selective CO_2 photoreduction to CH_4 under visible light. *Materials Research Bulletin*, **2021**, *137*: 111177.

[6] Li X, Sun Y, Xu J, et al. Selective visible-light-driven photocatalytic CO_2 reduction to CH_4 mediated by atomically thin $CuIn_5S_8$ layers. *Nature Energy*, **2019**, *4*(8): 690-699.

[7] He Y, Li C, Chen X-B, et al. Visible-light-responsive UiO-66(Zr) with defects efficiently promoting photocatalytic CO_2 reduction. *ACS Applied Materials & Interfaces*, **2022**, *14*(25): 28977-28984.

[8] Yu H, Chen F, Li X, et al. Synergy of ferroelectric polarization and oxygen vacancy to promote CO_2 photoreduction. *Nature Communications*, **2021**, *12*(1): 4594.

[9] Lu M, Liu J, Li Q, et al. Rational design of crystalline covalent organic frameworks for efficient CO_2 photoreduction with H_2O. *Angewandte Chemie International Edition*, **2019**, *58*(36): 12392-12397.

[10] Wang J, Heil T, Zhu B, et al. A single Cu-center containing enzyme-mimic enabling full photosynthesis under CO_2 reduction. *ACS Nano*, **2020**, *14*(7): 8584-8593.

[11] Shi X, Huang Y, Bo Y, et al. Highly selective photocatalytic CO_2 methanation with water vapor on single-atom platinum-decorated defective carbon nitride. *Angewandte Chemie International Edition*, **2022**, *61*(27): e202203063.

[12] Bi W, Hu Y, Jiang H, et al. Revealing the sudden alternation in Pt@h-BN nanoreactors for nearly 100% CO_2-to-CH_4 photoreduction. *Advanced Functional Materials*, **2021**, *31*(29): 2010780.

[13] Xin Z K, Gao Y J, Gao Y, et al. Rational design of dot-on-rod nano-heterostructure for photocatalytic CO_2 reduction: Pivotal role of hole transfer and utilization. *Advanced Materials*, **2022**, *34*(3): 2106662.

[14] Zhang M, Chang J N, Chen Y, et al. Controllable synthesis of COFs-based multicomponent nanocomposites from core-shell to yolk-shell and hollow-sphere structure for artificial photosynthesis. *Advanced Materials*, **2021**, *33*(48): 2105002.

[15] Dong L Z, Zhang L, Liu J, et al. Stable heterometallic cluster-based organic framework catalysts for artificial photosynthesis. *Angewandte Chemie International Edition*, **2020**, *59*(7): 2659-2663.

[16] Zhao Y, Han Z, Gao G, et al. Dual functions of CO_2 molecular activation and 4f levels as electron transport bridge in dysprosium single atom composite photocatalysts with enhanced visible-light photoactivities. *Advanced Functional Materials*, **2021**, *31*(38): 2104976.

[17] Chen E X, Qiu M, Zhang Y F, et al. Energy band alignment and redox-active sites in metalloporphyrin-spaced metal-catechol frameworks for enhanced CO_2 photoreduction. *Angewandte Chemie International Edition*, **2022**, *61*(1): e202111622.

[18] Wu H, Kong X Y, Wen X, et al. Metal–organic framework decorated cuprous oxide nanowires for long-lived charges applied in selective photocatalytic CO_2 reduction to CH_4. *Angewandte Chemie International Edition*, **2021**, *60*(15): 8455-8459.

[19] Wang L, Wang R, Qiu T, et al. Bismuth vacancy-induced efficient CO_2 photoreduction in BiOCl directly from natural air: A progressive step toward photosynthesis in nature. *Nano Letters*, **2021**, *21*(24): 10260-10266.